

A STEP TOWARD FLOW SIMULATION THROUGH CRACKS IN BEAM-PARTICLE MODELS

OMAR NAJJAR^{*,†}, THOMAS HEITZ[†], CÉCILE OLIVER-LEBLOND^{*}, JEAN-LOUIS TAILHAN[•], GIUSEPPE RASTIELLO[◊] AND FRÉDÉRIC RAGUENEAU^{*,‡}

* Université Paris-Saclay, ENS Paris-Saclay, CentraleSupélec, CNRS, LMPS - Laboratoire de Mécanique Paris-Saclay

91190, Gif-sur-Yvette, France

e-mail: omar.najjar@ens-paris-saclay.fr

† Autorité de Sûreté Nucléaire et de Radioprotection (ASNR), PSN-EXP/SES/LMAPS
F-92260, Fontenay-aux-Roses, France

‡ EPF École d'Ingénieurs
55 av. Président Wilson, F-94230, Cachan, France

• Université Gustave Eiffel - MAST/EMGCU
77447, Marne-la-Vallée Cedex 2, France

◊ Université Paris-Saclay, CEA, Service d'Études Mécaniques et Thermiques
91191, Gif-sur-Yvette, France

Key words: Crack Characterization, Beam-Particle Simulation, Discrete Element Method, Graph Theory, Air Leakage

Abstract. Crack characterization in reinforced concrete structures, such as the containment walls of 1300 MWe nuclear power plants, is critical for accurately estimating air leakage. Traditional modeling strategies, such as Poiseuille's law applied to a simplified geometry, rely on indirect parameters like a tortuosity coefficient, which is difficult to predict and has limited validity, leading to increased uncertainty. This study presents a novel post-processing tool based on the Beam-Particle simulation approach, capable of detecting micro-crack paths and constructing macro-crack geometries using graph theory. The generated macro-crack geometry can be integrated into computational fluid dynamics (CFD) simulations for more accurate airflow predictions or by calibrating simplified approaches like Poiseuille's law based on numerically obtained crack characteristics. Validation against optical measurements from Brazilian splitting tests demonstrates the tool's potential to advance simplified modeling and enhance detailed crack characterization, opening new possibilities for improved air leakage predictions.

1 INTRODUCTION

When leak-tightness performance is sought for reinforced concrete walls, like in nuclear reactor containment building, a quantitative assessment of leakage through cracks in accidental conditions is crucial [1]. The crack char-

acteristics such as roughness, tortuosity, and opening significantly influence fluid flow rates [2]. However, accurately characterizing crack geometry at the structural scale remains a significant challenge [2].

Two main approaches for crack characteri-

zation exist. Member-scale models, often based on simplified geometries and modifications of Poiseuille's law, are widely used but require recalibration for varying concrete types and loading conditions [3]. These models provide a basic estimate of flow rates, though they lack detailed crack descriptions. In contrast, crack-scale models utilize detailed simulations, including CFD, to estimate fluid flow through complex crack geometries [4], although experimental methods are often impractical for large-scale applications.

This paper proposes a novel method to characterize concrete cracks using graph theory applied to Discrete Element Analysis Program (DEAP) mechanical simulations [5], coupled with CFD for fluid flow estimation. This tool represents a part of comprehensive work that will be made for a full-chain model, which includes a weak coupling between the Finite Element Method (FEM) and the DEAP discrete model to reduce the computational cost of the DEAP model as proposed by [6], which will be presented in future studies. A Brazilian splitting test case study validates this approach, comparing simulation results with experimental data and demonstrating its potential for practical applications.

2 CRACK CHARACTERISTICS

Crack characteristics such as opening, tortuosity, and roughness significantly influence flow rate. Below is a summary of each.

2.1 Crack Opening

The crack opening e is a critical parameter that significantly influences the flow rate through the crack, scaling cubically as $Q \propto e^3$, as shown in Equation 1. This relationship is derived from the fluid continuity equation, assuming a compressible ideal gas with laminar flow between two parallel plates (Poiseuille-type flow) and constant temperature. It highlights the sensitivity of the flow rate to changes in the crack aperture.

$$Q = \frac{be^3}{24\mu} \frac{M}{R_{pg}T} \frac{P_1^2 - P_2^2}{l}, \quad (1)$$

where Q is the mass flow rate, b is the crack width, μ is the dynamic viscosity, M is the molar mass, R_{pg} is the specific gas constant, T is the temperature, P_1 and P_2 are the inlet and outlet pressures, respectively, and l is the crack length.

Various approaches have been proposed for defining the crack opening, such as the vertical distance between surfaces or the perpendicular distance to the local centerline. In this study, the vertical distance between the crack surfaces is employed for simplicity and consistency.

2.2 Tortuosity and Roughness

Tortuosity describes large-scale fluctuations in the crack surface, while roughness refers to smaller-scale variations. Both contribute to flow reduction, typically by a factor of 4 to 6 [2]. Tortuosity is defined as the ratio of the effective length l_{eff} to the actual length l :

$$\tau = \frac{l_{eff}}{l}, \quad (2)$$

where the effective length l_{eff} represents the geometrical path of the crack, capturing deviations caused by surface irregularities.

Roughness, on the other hand, quantifies the small-scale surface deviations from the mean surface and is represented by the average roughness R_a . The mathematical definition of R_a is given as:

$$R_a = \frac{1}{l_m} \int_{x=0}^{l_m} |y(x)| dx, \quad (3)$$

where l_m is the sampling length, and $y(x)$ represents the surface profile as a function of x .

Figure 1 illustrates the concept of average roughness. Here, R_a measures the mean absolute deviation of the surface profile from its average line over the length l_m . While roughness significantly influences the local flow dynamics, its effects are typically smaller compared to tortuosity on a larger scale. This study focuses

on representing tortuosity rather than roughness due to the absence of roughness characterization in the presented tool.

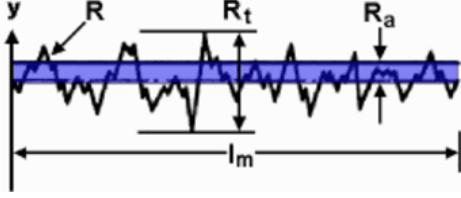


Figure 1: Average roughness.

3 METHODOLOGY

The methodology followed in this study consists of two main steps: first, crack pattern modeling using the DEAP model [5], and second, 3D macro-crack extraction. A brief explanation of the approach adopted in this study is provided below.

3.1 DEAP BEAM-PARTICLE MODEL

The beam-particle model, as illustrated in [5], combines lattice and discrete element methods to analyze concrete failure. The model represents the material as a network of polygonal particles connected by brittle beams, which simulate cohesive forces. When the material deforms or fails, the beams break according to specific fracture criteria, forming micro-cracks that link to create larger macro-crack patterns Figure 2. Micro-cracks correspond to the facets between particles, and the progressive connection of these micro-cracks reproduces tortuous crack paths. The random spatial distribution of particle connections and failure thresholds captures the heterogeneous nature of concrete, reflecting the energy dissipation and crack propagation observed in experiments. These features enable the model to simulate realistic failure patterns under tensile and compressive loads [7]. To capture the quasi-brittle nature of the material, a fracture criterion is defined for the beam connecting particles. The breaking threshold B_{ij} depends on the axial strain and rotational difference between the two particles and is expressed as:

$$B_{ij} = \left(\frac{\varepsilon_{ij}}{\varepsilon_{ij}^{cr}} \right) + \left(\frac{|\theta_i - \theta_j|}{\theta_{ij}^{cr}} \right), \quad (4)$$

where ε_{ij}^{cr} and θ_{ij}^{cr} are the critical strain and rotational limits for the beam connecting particles i and j , respectively, and the strain is calculated as $\varepsilon_{ij} = \frac{u_i - u_j}{l_{b,ij}}$.

The fracture occurs when the threshold B_{ij} exceeds unity:

$$B_{ij} > 1. \quad (5)$$

Here, $B_{ij} > 1$ represents the condition for failure, where the combined normalized strain and rotational difference exceed the critical limits of the beam. This formulation ensures that the fracture criterion captures both axial deformation and rotational effects. When this criterion is met, the beam is considered to have failed and is removed from the system and the joint surface between both particles is considered as a crack. The particles themselves are treated as undeformable and unbreakable, with the beam being the only component subject to failure.

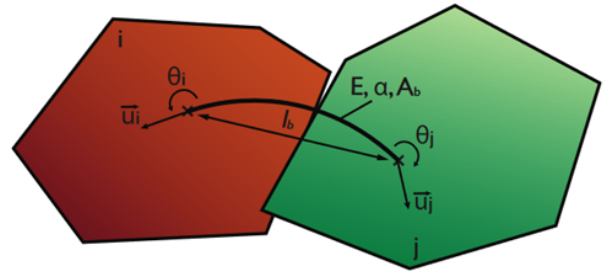


Figure 2: Illustration of two cohesively linked particles, showing brittle beams connecting particle centroids and cohesive forces acting at the interface [7]

The crack opening e_{ij} is defined along a vector parallel to the initial line of the beam in its original state without any loading, as follows:

$$e_{ij} = \langle (\underline{u}_j - \underline{u}_i) \cdot \underline{n}_{ij} \rangle_+ \quad (6)$$

where \underline{n}_{ij} is the normal vector to the initial interface surface linking the two particles.

3.2 3D Macro-crack Generation

The cracking patterns obtained from the DEAP model can be analyzed using graph theory, as described in [5], by examining both the displacement field and the network of micro-cracks. The graph is represented by an adjacency matrix that identifies connections between nodes, with distances and predecessors calculated to analyze the connectivity and structure of the micro-crack network.

The positions of micro-crack vertices are determined from particle displacements under small deformation assumptions. However, when multiple cracks share a vertex, their positions are calculated independently, leading to discrepancies where the shared vertex does not coincide, as illustrated in Figure 3. This issue highlights the need for a more coherent macro-crack geometry.

To address this, a new post-processing tool was developed to construct a structured macro-crack geometry compatible with CFD simulations. The tool applies graph theory to identify connected micro-cracks and evaluates their relevance based on criteria such as crack openings and the number of micro-cracks along each path. The connected components are filtered and merged into larger, coherent structures. Figure 4 illustrates an example network of micro-cracks, showing the largest connected components, the longest simple paths contributing to flow (red), non-contributing paths (blue), and isolated cracks (black). This visual representation demonstrates how the tool integrates graph theory into generating macro-crack geometries.

Once the paths are identified, a smoothing function is applied to ensure the generated crack surfaces are continuous and suitable for meshing. A Locally Weighted Scatterplot Smoothing (LOWESS) [8] function is used, defined as:

$$\hat{z}_i = \arg \min_{z_i} \sum_{j=1}^n w_{ij} (z_j - \beta_0 - \beta_1(x_j - x_i) - \beta_2(y_j - y_i))^2 \quad (7)$$

where, w_{ij} are weights defined by a kernel func-

tion that decreases with distance from the target point (x_i, y_i) , β_0 , β_1 , and β_2 are coefficients of the local linear model, and n is the number of data points in the neighborhood. This method ensures a smooth transition across the crack surface while preserving critical features.

Finally, the Python-based Gmsh tool [9] generates a 3D mesh of the fitted crack surfaces, ensuring compatibility with CFD software such as ANSYS CFX [10]. This approach produces an accurate and physically representative macro-crack structure by incorporating both displacement data and the micro-crack network topology, resolving the issue of independent vertex positions for improved flow simulations.

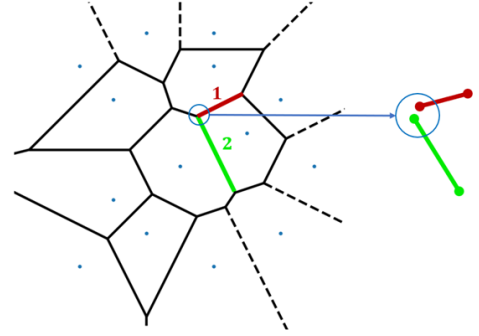


Figure 3: Two neighboring cracks sharing a vertex, calculated independently for each crack.

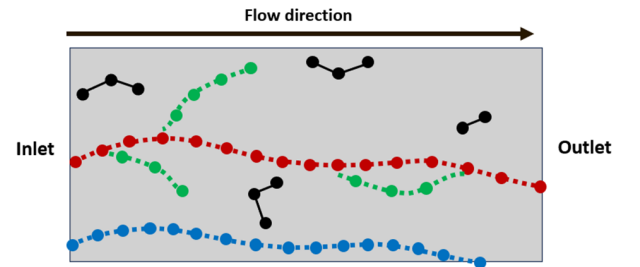
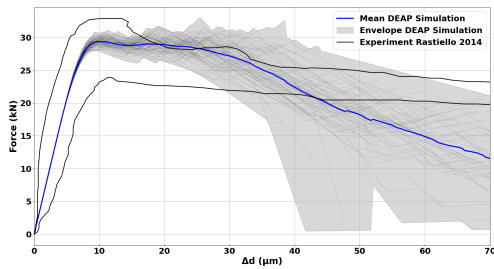


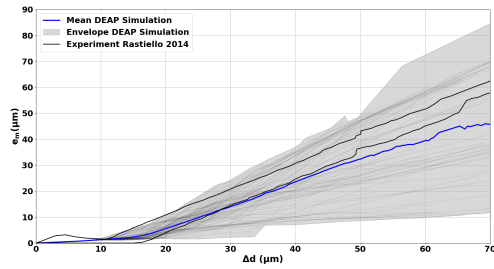
Figure 4: Representation of the networks of micro-cracks: extraction of the largest connected component (red + green), the longest simple path contributing to flow rate (red), the longest simple path not contributing to flow rate (blue, assuming the lower side is impermeable) and isolated micro-cracks (black) with graph theory.

4 BRAZILIAN SPLITTING TEST CASE STUDY

The DEAP model was validated against experimental data from [3], which examined the relationship between permeability and crack width in saturated concrete using Brazilian splitting tests. The concrete sample had dimensions and properties as previously mentioned, with $f_t = 3.36$ MPa, $E = 41.7$ GPa, and $\nu = 0.20$. Figure 5 compares 80 DEAP simulations with experimental results for force vs. diameter change and crack opening vs. diameter change. The model shows good agreement with experiments, particularly in capturing tensile strength. Variations beyond $\Delta d = 35 \mu\text{m}$ are due to macro-crack formation leading to failure. The developed tool was applied to the DEAP simulation of the Brazilian splitting test.



(a) Force vs change of diameter

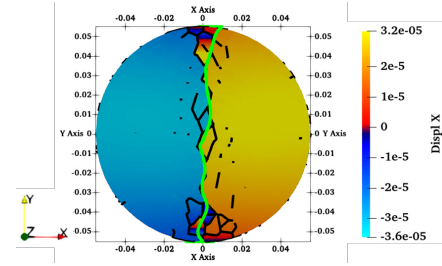


(b) Crack opening vs change of diameter

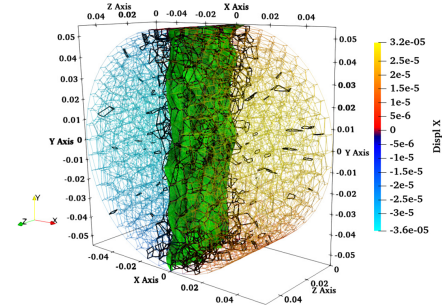
Figure 5: Comparison of DEAP simulations with envelope experimental results: (a) Force vs. diameter change, (b) Crack opening vs. diameter change.

Figure 6 shows the displacement field along the x -axis, with micro-cracks (black) appearing at $t_i = 85$ ($\Delta d \approx 70 \mu\text{m}$) and the extracted macro-crack volume (green). The macro-crack closely follows the connected micro-cracks in

the specimen's center, with small disturbances near the boundaries.



(a) 2D view



(b) 3D view

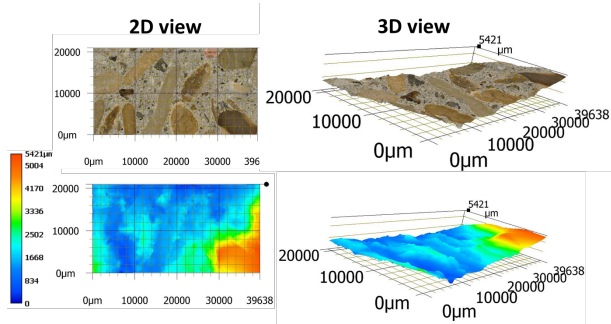
Figure 6: Results of the Brazilian splitting test showing the displacement field in the X direction, with micro-cracks (black) and the extracted macro-crack (green): (a) 2D views; (b) 3D view.

To compare with real crack characteristics, optical topography measurements were performed on the Brazilian concrete splitting test samples from [11], which studied real-time air-flow through concrete cracks. A VHX-7000 optical machine with $\times 100$ magnification ($1.5 \mu\text{m}/\text{pixel}$ resolution) was used for measurements. This method also allows the assessment of roughness levels to be modeled within the crack. The sample was cylindrical, with a diameter of $D = 110 \text{ mm}$ and thickness $l = 50 \text{ mm}$. The optical measurements were made on a representative zone of $2 \text{ cm} \times 4 \text{ cm}$ in size. Several measurements were taken, covering the entire crack. Since the machine cannot measure the whole surface at once, the area was divided into smaller regions for sampling. The zone presented in this study has been chosen because it is free from artifacts that could create peaks

in the elevation measurements, thereby reducing the need for additional processing. The optical measurement results, illustrated in Figure 7, provide a detailed representation of the analyzed surface. The related 3D reconstruction reveals the fluctuations in surface elevation, showing the roughness patterns and microscopic height disparities.



(a) Sample and top view of the analyzed zone. The highlighted region represents the area of focus for surface characterization.



(b) 3D reconstruction and topographic mapping of the selected zone. The elevation map illustrates surface elevation in μm .

Figure 7: Optical measurements of a representative zone approximately $2\text{ cm} \times 4\text{ cm}$ in size.

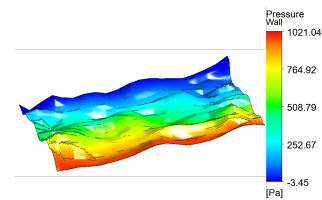
The macro-crack characteristics, including tortuosity in the Y and Z directions, as well as crack opening statistics, are summarized in Table 1. The fitting parameters for the macro-crack are calibrated using experimental data obtained from optical measurements. The analysis highlights that fluctuations near the top and bottom boundaries contribute significantly to the variations observed when considering the whole region of the macro-crack. It is evident that by focusing on the middle region in the DEAP simulations, the results align more closely with the experimental data. This demonstrates the tool's reliability when boundary-induced fluctuations are excluded from the analysis. The deviations

in the Z direction for the whole region are attributed to these surface fluctuations, which significantly influence the measurements near the

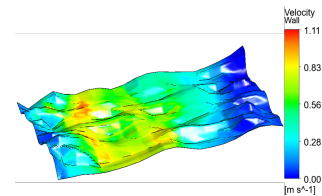
boundaries. Additionally, Table 1 includes information about the crack opening characteristics obtained from the DEAP simulations, such as mean, minimum, and maximum values. The obtained macro-crack has been used as input for CFD simulations. Detailed results will be presented in future studies. Figure 8 provides an overview of airflow simulation using the ANSYS CFX 2022 program as a proof of concept for the application of the tool. The figure illustrates the pressure field for a relative pressure of 1000 Pa applied at the inlet and atmospheric pressure at the outlet, as well as the velocity field for the layer near the walls of the obtained macro-crack.

Table 1: Comparison of experimental and DEAP simulation tortuosity data and crack opening statistics.

Parameter	DEAP Simulation		Experimental
	Whole region	Middle region	
$\tau_{y,mean}$	1.0609 ± 0.0251	1.0473 ± 0.0231	1.0640 ± 0.0241
$\tau_{z,mean}$	1.2540 ± 0.1979	1.0924 ± 0.0390	1.0854 ± 0.0131
e_{mean} (μm)	42.72 ± 17.20	–	–
e_{min} (μm)	0.7462	–	–
e_{max} (μm)	64.32	–	–



(a) Pressure field



(b) Velocity field

Figure 8: CFD simulation results showing (a) the pressure field and (b) the velocity field.

5 Conclusions

This study has demonstrated the effectiveness of the newly developed strategy in capturing a detailed description of concrete macro-cracks, including their length, tortuosity, and variations in crack opening. Additionally, the approach enables the integration of complex CFD simulations through these geometries, laying the groundwork for future studies.

The presented tool provides a critical step toward simulating the leakage behavior of large structures by accurately characterizing macro-cracks. Future work will focus on integrating this approach with global models, as demonstrated in [6], to explore its full potential in real-world scenarios, particularly for large-scale structural analyses. This integration aims to improve the accuracy of airflow estimations and provide a more comprehensive understanding of leakage mechanisms.

REFERENCES

- [1] B. Masson, E. Galenne, E. Oukhemanou, C. Aubry, and G. Laou-Sio-Hoi. Vercors: a 1/3 scaled mockup and an ambitious research program to better understand the different mechanisms of leakage and aging. France, 2015. INIS Reference Number: 46081735.
- [2] Alireza Akhavan, Seyed-Mohammad-Hadi Shafaatian, and Farshad Rajabipour. Quantifying the effects of crack width, tortuosity, and roughness on water permeability of cracked mortars. *Cement and Concrete Research*, 42(2):313–320, 2012.
- [3] G. Rastiello, C. Boulay, S. Dal Pont, J. L. Tailhan, and P. Rossi. Real-time water permeability evolution of a localized crack in concrete under loading. *Cement and Concrete Research*, 56:20–28, February 2014.
- [4] R. Zimmerman and In-Wook Yeo. Fluid flow in rock fractures: From the Navier-Stokes equations to the Cubic Law. *Washington DC American Geophysical Union Geophysical Monograph Series*, 122:213–224, January 2000.
- [5] C. Oliver-Leblond. Discontinuous crack growth and toughening mechanisms in concrete: A numerical study based on the beam-particle approach. *Engineering Fracture Mechanics*, 207:1–22, February 2019.
- [6] Cécile Oliver-Leblond, Arnaud Delaplace, Frédéric Ragueneau, and Benjamin Richard. Non-intrusive global/local analysis for the study of fine cracking: global/local analysis for fine cracking in concrete. *International Journal for Numerical and Analytical Methods in Geomechanics*, 37(8):973–992, June 2013.
- [7] M. Vassaux, C. Oliver-Leblond, B. Richard, and F. Ragueneau. Beam-particle approach to model cracking and energy dissipation in concrete: Identification strategy and validation. *Cement and Concrete Composites*, 70:1–14, July 2016.
- [8] William S. Cleveland. Robust Locally Weighted Regression and Smoothing Scatterplots. *Journal of the American Statistical Association*, 74(368):829–836, 1979. Publisher: [American Statistical Association, Taylor & Francis, Ltd.].
- [9] Christophe Geuzaine and Jean-François Remacle. Gmsh: A 3-D Finite Element Mesh Generator with Built-in Pre- and Post-Processing Facilities. *International Journal for Numerical Methods in Engineering*, 79:1309–1331, September 2009.
- [10] Inc Ansys. ANSYS CFX-Solver Theory Guide Release 2022-R1, 2022.
- [11] Jean-Louis Tailhan, Giuseppe Rastiello, Jean-Claude Renaud, and Claude Boulay. An experimental test for gas pressure measurement within a realistic crack in concrete. *Nuclear Engineering and Design*, 403:112138, March 2023.